arXiv:1606.06946v1 [math.CA] 22 Jun 2016

Numerics for the spin orbit equation of Makarov with constant eccentricity

Michele Bartuccelli[1], **Jonathan Deane**[1], **Guido Gentile**[2]

[1] Department of Mathematics, University of Surrey, Guildford, GU2 7XH, UK

[2] Dipartimento di Matematica e Fisica, Università di Roma Tre, Roma, I-00146, Italy

E-mail: m.bartuccelli@surrey.ac.uk, j.deane@surrey.ac.uk, gentile@mat.uniroma3.it

Abstract

We present an algorithm for the rapid numerical integration of a time-periodic ODE with a small dissipation term that is C^1 in the velocity. Such an ODE arises as a model of spin-orbit coupling in a star/planet system, and the motivation for devising a fast algorithm for its solution comes from the desire to estimate probability of capture in various solutions, via Monte Carlo simulation: the integration times are very long, since we are interested in phenomena occurring on times similar to the formation time of the planets. The proposed algorithm is based on the High-order Euler Method (HEM) which was described in [Bartuccelli et al. (2015)], and it requires computer algebra to set up the code for its implementation. The pay-off is an overall increase in speed by a factor of about 7.5 compared to standard numerical methods. Means for accelerating the purely numerical computation are also discussed.

1 Introduction

The paper first concisely sets out the model for spin-orbit coupling in, for instance, the Sun-Mercury system, as described by Makarov [Makarov (2012)] and further discussed by Noyelles, Frouard, Makarov and Efroimsky in [Noyelles et al. (2014)]. We refer to this model as the NFME model throughout. We then describe a fast numerical algorithm, based on the High-order Euler Method (HEM) introduced in [Bartuccelli et al. (2015)], for solving the spin-orbit ODE incorporating the NFME model. After rigorous testing, we conclude that the proposed algorithm is about 7.5 times faster than simply using a general-purpose numerical ODE solver.

There are two main reasons for developing a fast algorithm for solving this version of the spin-orbit ODE, bearing in mind that the ultimate objective is to establish, by Monte Carlo simulation, the probability of capture in the various attracting solutions of the ODE. The first reason is that, since the dissipation in the problem is low, very long integration times — of the order of that of the formation of the planets — are needed in order to establish capture. The second reason is that to estimate capture probabilities with high confidence, solutions starting from many randomly-chosen initial conditions need to be considered: in fact, the width of the confidence interval decreases only as the square root of the number of solutions investigated. In most of the previous related work, for instance, [Correia and Laskar (2004)], [Celletti and Chierchia (2008)], [Makarov (2012)], [Makarov et al. (2012)], only about 1000 initial conditions were considered. By contrast, we are able to consider more than 50,000 here, for which the total computation time is of order two weeks.

The dynamics of the solutions of the spin-orbit ODE with the NFME model are also interesting, and we discuss these in a separate paper [Bartuccelli et al. (in preparation)].

In [Noyelles et al. (2014)], the authors point out how the model that they advocate describes more realistically the effect of tidal dissipation, in comparison with the much simpler constant time-lag (CTL) model. The latter has been used extensively in the literature since the seminal paper by Goldreich and Peale [Goldreich and Peale (1966)] — see for instance [Correia and Laskar (2004)], [Celletti and Chierchia (2008)], [Celletti and Chierchia (2009)] and [Bartuccelli et al. (2015)] for recent results on the basins of attraction of

the principal attractors. A clear drawback of the CTL model is that, for the parameters of the Sun-Mercury system, the main attractor (with 70% probability of being observed) is quasi-periodic, with an approximate frequency of 1.256. In fact, Mercury is in a 3:2 spin-orbit resonance, and the CTL model indicates that the probability of this is only about 8%. On the other hand, with the NFME model, all attractors have mean velocity close to rational values, and about 42% of the initial data are captured by an attractor with mean velocity close to 3/2.
The greater realism of the NFME model comes at a cost, however:

1. The NFME model is not smooth; in fact, it is only C^1 in the angular velocity, $\dot{\theta}$, as we shall see.
2. There is considerable detail to take into account in implementing the NFME model mathematically.
3. The functions in the model take considerably more computation time to evaluate, and so numerical calculations are comparatively slow.

The first point is important both for application of perturbation theory to the problem as well as for implementing an appropriate fast HEM-type algorithm to solve the ODE. Both of these objectives are important. For instance, perturbation theory is a useful tool for obtaining any kind of analytical results for the dynamics; and the motivation for faster algorithms has already been discussed above.
Throughout this paper, the units for mass, length and time will be kg, km and Earth years, yr, respectively. For ease of cross-referencing, an equation numbered (N.x) in this paper is equation (x) in [Noyelles et al. (2014)], modified if necessary. When we refer to a 'standard numerical method' or 'numerical method' for ODE solving, we mean one of the family of well-known general purpose ODE solvers (e.g. Runge-Kutta, Adams); when we mean HEM, which is of course also numerical, we refer to it explicitly by name.

2 The NFME model

2.1 The spin-orbit ODE

The ODE is

$$\ddot{\theta} = \frac{\mathcal{T}_z^{\mathrm{TRI}}(\theta, t) + \mathcal{T}_z^{\mathrm{TIDE}}(\dot{\theta})}{\xi M_{planet} R^2} \tag{N.1}$$

where ξ is a measure of the inhomogeneity of the planet (with $\xi = 2/5$ for a homogeneous sphere), M_{planet} is the mass of the planet and R is its radius. Numerical values for these, and indeed all relevant parameters can be found in Table 1.

2.2 The triaxiality torque

The triaxiality-caused torque along the z-axis, $\mathcal{T}_z^{\mathrm{TRI}}(\theta, t)$, is a torque exerted on the planet by the gravitational field of the star, arising from the fact that the planet is not a perfect sphere. Goldreich and Peale [Goldreich and Peale (1966)] and NFME approximate $\mathcal{T}_z^{\mathrm{TRI}}$ by its quadrupole part, which is given by

$$\mathcal{T}_z^{\mathrm{TRI}} \approx -\frac{3a^3}{2r^3}(B-A)n^2 \sin 2(\theta - f) = -\frac{3a^3}{2r^3}(B-A)n^2(\sin 2\theta \cos 2f - \cos 2\theta \sin 2f) \tag{N.5}$$

where the principal moments of inertia of the planet, along the x, y and z axes respectively, are $A < B < C = \xi M_{planet} R^2$; n is its mean motion; $r = r(t)$ is the distance between the centres of mass of the star and the planet at time t; a is the semi-major axis of the orbit of the planet; $\theta(t)$ is the sidereal angle of the planet, measured from the major axis of its orbit; and $f = f(t)$ is the true anomaly as seen from the star. We further define $\mathcal{M}(t)$, the mean anomaly, which is such that $n = \dot{\mathcal{M}}$, with a good approximation [Noyelles et al. (2014)]

being given by[1] $n \approx \sqrt{G(M_{planet}+M_{star})/a^3}$, where G is the gravitational constant and M_{star} is the mass of the star. Hence, aside from a constant of integration which we set to zero, $\mathcal{M} = nt$.
The standard procedure from this point is to make the following pair of Fourier expansions:

$$\left(\frac{r(t)}{a}\right)^n \begin{matrix}\cos\\ \sin\end{matrix} (mf(t)) = \sum_{k\in\mathbb{Z}} X_k^{n,m}(e) \begin{matrix}\cos\\ \sin\end{matrix} (knt) \tag{N.7, N.8}$$

where $X_k^{n,m}(e)$ are the Hansen coefficients, which depend on the orbital eccentricity e. NFME compute them via [Duriez (2007)]

$$X_k^{n,m}(e) = (1+z^2)^{-n-1} \sum_{g=0}^{\infty} (-z)^g \sum_{h=0}^{g} C_{g-h,h}^{n,m}\, J_{k-m+g-2h}(ke), \tag{N.9}$$

where $z = (1-\sqrt{1-e^2})/e$, $J_k(x)$ is the k-th order Bessel function of the first kind, and

$$C_{r,s}^{n,m} = \begin{pmatrix} n+1+m \\ r \end{pmatrix} \begin{pmatrix} n+1-m \\ s \end{pmatrix}$$

with the binomial coefficients (extended to all integer arguments) being given by

$$\begin{pmatrix} l \\ m \end{pmatrix} = \begin{cases} \frac{l(l-1)\ldots(l-m+1)}{m!} & l\in\mathbb{Z}, m \geq 1 \\ 1 & l\in\mathbb{Z}, m = 0 \\ 0 & l\in\mathbb{Z}, m < 0. \end{cases}$$

For convenience, we define the functions $G_{lpq}(e) = X_{l-p+q}^{-l-1,\,l-2p}$. Then finally,

$$\mathcal{T}_z^{\mathrm{TRI}}(\theta,t) = -\frac{3}{2}(B-A)n^2 \sum_{q\in\mathbb{Z}} G_{20q}(e)\sin(2\theta-(q+2)nt). \tag{N.10}$$

In practice, NFME sum over $q \in \mathcal{Q}^{\mathrm{TRI}} = \{-4,\ldots,6\}$.

2.3 The tidal torque

NFME forcefully point out the problems associated with the constant time-lag (CTL) model, which leads to a dissipation term of the form $\gamma(\dot\theta-\omega)$, with γ and ω constants. This model, among other things, can give rise to quasi-periodic solutions for the spin-orbit problem [Correia and Laskar (2004), Celletti and Chierchia (2009), Bartuccelli et al. (2015)], and the fact that these have not been observed in practice is evidence that the CTL model is in some way unphysical.
NFME model tidal dissipation by expanding both the tide-raising potential of the star, and the tidal potential of the planet, as Fourier series. The Fourier modes are written ω_{lmpq}, where l,m,p,q are integers. Appendix B of [Noyelles et al. (2014)] justifies the simplification $l=m=2$, $p=0$, which arises from the smallness of the obliquity of the orbit (axial tilt), in combination with an averaging argument. This then gives the following approximation for the polar component of the tidal torque:

$$\mathcal{T}_z^{\mathrm{TIDE}}(\dot\theta) = \frac{3GM_{star}^2}{2a}\left(\frac{R}{a}\right)^5 \sum_{q,j\in\mathcal{Q}^{\mathrm{TIDE}}} G_{20q}(e)G_{20j}(e)Q_2(\omega_{220q})\,\mathrm{sgn}(\omega_{220q})\cos[(q-j)\mathcal{M}]. \tag{N.11a}$$

Here, $\mathcal{Q}^{\mathrm{TIDE}} = \{-1,\ldots,7\}$; $Q_2(\omega_{220q}) = k_2(\omega_{220q})\sin|\epsilon_2(\omega_{220q})|$, where both k_2 (a positive definite, even function of the mode ω_{lmpq}) and ϵ_2 (an odd function of the mode) are functions to be given shortly; and sgn() is the usual signum function. Hence, overall, $Q_2(x)\,\mathrm{sgn}(x)$ is an *odd* function of x. The reason why

[1] Numerically, this is true: [Noyelles et al. (2014)] give $n = 26.0879$ yr^{-1} for Mercury and the approximation yields $n \approx 26.0897$ yr^{-1}.

Q_2 is written in this form is that it will turn out to depend on a *fractional power* of $|\omega_{lmpq}|$: the oddness of $Q_2(x)\,\mathrm{sgn}(x)$ is thereby retained without raising a negative number to this fractional power.
The additive error terms for this expression are $O(e^8\epsilon)$, $O(i^2\epsilon)$ and $O\left(\epsilon R^7/a^7\right)$, in which i is the obliquity of the orbit and ϵ, which is $O(1)$, is a phase lag. For Mercury, $e^8 \approx 10^{-8}$, $i^2 \approx 10^{-7}$ and $(R/a)^7 \approx 10^{-31}$. NFME then make the additional approximation that, since the terms with $q \neq j$ oscillate, they naturally affect the detailed dynamics of the planet, but nonetheless, the overall capture probabilities are insensitive to them [Makarov et al. (2012)]. Hence, the tidal torque is well approximated by the secular part only, i.e. the $q = j$ terms; this gives

$$\mathcal{T}_z^{\mathrm{TIDE}}(\dot\theta) = \langle \mathcal{T}_z^{\mathrm{TIDE}}(\dot\theta)\rangle_{l=2} = \frac{3GM_{star}^2}{2a}\left(\frac{R}{a}\right)^5 \sum_{q\in\mathrm{Q}^{\mathrm{TIDE}}} G_{20q}^2(e)\,Q_2(\omega_{220q})\,\mathrm{sgn}(\omega_{220q}). \tag{N.11b}$$

Neglecting precessions, we have

$$\omega_{lmpq} = (l-2p+q)n - m\dot\theta \tag{N.12}$$

with $l \geq 2$, $m, p = 0, \ldots, l$ and $q \in \mathbb{Z}$. For the reasons mentioned earlier, we consider only the mode $\omega_{220q} = (q+2)n - 2\dot\theta$.
Finally, we give the NFME model for the quality function, $Q_2(\omega_{lmpq})$. We use the abbreviation $\chi = |\omega_{lmpq}|$, in terms of which

$$Q_2(\omega_{lmpq}) = -\frac{3A_l}{2(l-1)}\frac{I'(\chi)\chi}{(\mathcal{R}'(\chi)+A_l\chi)^2 + I'(\chi)^2}, \tag{N.15 mod.}$$

where

$$A_l = \frac{4\pi(2l^2+4l+3)\mu R^4}{3lGM_{planet}^2},$$

with μ being the unrelaxed rigidity;

$$\mathcal{R}'(\chi) = \chi + \chi^{1-\alpha}\tau_A^{-\alpha}\cos(\alpha\pi/2)\,\Gamma(\alpha+1) \tag{N.16 mod.}$$

and

$$I'(\chi) = -\tau_M^{-1} - \chi^{1-\alpha}\tau_A^{-\alpha}\sin(\alpha\pi/2)\,\Gamma(\alpha+1). \tag{N.17 mod.}$$

In these expressions, Γ is the usual gamma function, τ_A and τ_M are the Andrade and Maxwell times of the mantle respectively and α is the Andrade parameter.

2.4 Parameter values for the Sun/Mercury system

In Table 1 we give numerical values appropriate to the Sun and Mercury for the parameters introduced so far. We standardise the units to kg for mass, km for length and (Earth) years for time.

2.5 The triaxiality and tidal angular accelerations

In order to study the spin-orbit problem further, it is convenient to introduce two quantities with the dimensions of angular acceleration

$$\ddot\theta^{\,\mathrm{TRI}}(\theta,t) = \mathcal{T}_z^{\mathrm{TRI}}(\theta,t)/\xi M_{planet}R^2 \quad \text{and} \quad \ddot\theta^{\,\mathrm{TIDE}}(\dot\theta) = \mathcal{T}_z^{\mathrm{TIDE}}(\dot\theta)/\xi M_{planet}R^2.$$

Taken individually, these quantities are not accelerations *per se* — more correctly, they might be described as the triaxiality/tidal contributions to the angular acceleration, since, when computed on the solution $\theta(t)$, their sum is $\ddot\theta$, as we shall see from equation (3) — but for brevity, we refer to them as the triaxiality and tidal accelerations. We then define

$$\zeta = \frac{3(B-A)n^2}{2\xi M_{planet}R^2} \approx 0.09545\ \mathrm{yr}^{-2} \quad \text{so that} \quad \ddot\theta^{\,\mathrm{TRI}}(\theta,t) = -\zeta\sum_{q\in\mathrm{Q}^{\mathrm{TRI}}} G_{20q}(e)\sin(2\theta-(q+2)nt), \tag{1}$$

Parameter values specific to Mercury		
Name	Symbol	Numerical value
Semimajor axis	a	5.791×10^7 km
Mean motion	n	26.0879 rad yr^{-1}
Planetary radius	R	2.44×10^3 km
Dimensionless m.o.i. (inhomogeneity)	$\xi = C/(M_{planet}R^2)$	0.346
Triaxiality	$(B-A)/C$	9.350×10^{-5}
Planetary mass	M_{planet}	3.301×10^{23} kg
Unrelaxed rigidity	μ	7.967×10^{28} kg km^{-1} yr^{-2}
Present-day orbital eccentricity	e	0.2056
Andrade time	τ_A	500 yr
Maxwell time	τ_M	500 yr
Andrade parameter	α	0.2
Acceleration constants		
Triaxiality acceleration constant	ζ	0.09545 yr^{-2}
Tidal acceleration constant	η	0.03096 yr^{-2}
Other parameter values		
Mass of Sun	M_{star}	1.989×10^{30} kg
Gravitational constant	G	6.646×10^{-5} kg^{-1} km^3 yr^{-2}
Triaxiality index range	$\mathcal{Q}^{\mathrm{TRI}}$	$\{-4, \ldots, 6\}$
Tidal index range	$\mathcal{Q}^{\mathrm{TIDE}}$	$\{-1, \ldots, 7\}$

Table 1: Numerical values for the parameters used in the NFME model for the Sun and Mercury.

and

$$\eta = \frac{3GM_{star}^2R^5}{2a^6\xi M_{planet}R^2} \cdot \frac{3A_l}{2(l-1)} = \frac{3\pi(2l^2+4l+3)}{l(l-1)} \frac{\mu M_{star}^2R^7}{\xi M_{planet}^3 a^6} \approx 0.03096 \text{ yr}^{-2}$$

for $l = 2$, so that

$$\ddot{\theta}^{\,\mathrm{TIDE}}(\dot{\theta}) = -\eta \sum_{q \in \mathcal{Q}^{\mathrm{TIDE}}} G_{20q}^2(e) P_2\left(|\omega_{220q}|\right) \mathrm{sgn}(\omega_{220q}) \tag{2}$$

where

$$P_2(\chi) = \frac{\mathit{I}'(\chi)\chi}{(\mathcal{K}'(\chi) + A_2\chi)^2 + \mathit{I}'(\chi)^2}$$

and $\mathcal{K}'(\chi)$ and $\mathit{I}'(\chi)$ are defined in equation (N.17 mod.).
In terms of these angular accelerations, the spin-orbit ODE becomes

$$\ddot{\theta} + \zeta \sum_{q \in \mathcal{Q}^{\mathrm{TRI}}} G_{20q}(e) \sin(2\theta - (q+2)nt) + \eta \sum_{q \in \mathcal{Q}^{\mathrm{TIDE}}} G_{20q}^2(e) P_2\left(\left|2\dot{\theta} - (q+2)n\right|\right) = 0 \tag{3}$$

and this is our starting point for the rest of the paper.

3 The NFME model with practical values

We now look at the behaviour and magnitude of the various functions that go to make up the NFME model, using the values for the Sun and Mercury given in the Table 1.

3.1 Hansen coefficients

In figure 1 we plot the Hansen coefficients relevant to the problem, $G_{20q} = X_{q+2}^{-3,2}$, for $e = 0.2056, 0.3$ and 0.4 and for $q = -12, \ldots, 12$. These were computed from equation (N.9) by truncating the first sum at $p = 120$

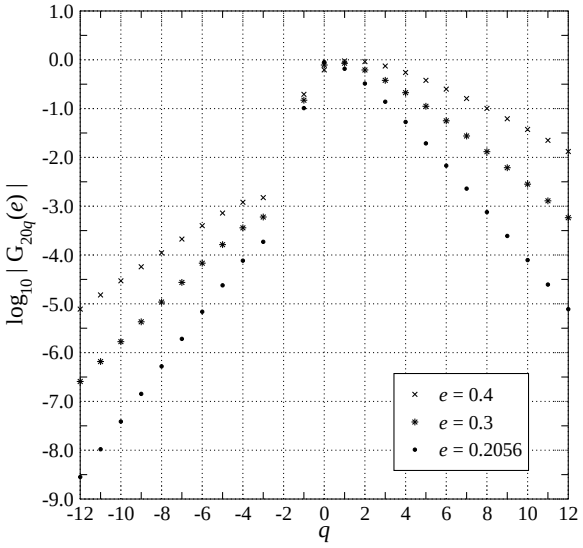

Figure 1: Plot of $\log_{10}|G_{20q}(e)|$ for $e = 0.2056, 0.3, 0.4$ (the latter two values being for illustration) and $q = -12, \ldots, 12$. Note that, for all values of e considered, (i) only $G_{2,0,-1}$ is negative, and (ii) $G_{2,0,-2} = 0$ and is therefore not plotted.

and using 20 significant figures for computation — these values allow the computation of the coefficients to a much higher precision than necessary.

3.2 The triaxiality acceleration

We first make a simple estimate of the order of magnitude of $\ddot{\theta}^{\,\mathrm{TRI}}(\theta, t)$. Treating θ and t as independent variables, it is clear from equation (N.10) that $\ddot{\theta}^{\,\mathrm{TIDE}} \in [-D, D]$ for all θ, t, where

$$D(e) = \zeta \sum_{q \in Q^{\mathrm{TRI}}} |G_{20q}(e)| \,. \tag{4}$$

We find $D(0.2056) = 0.2096$, $D(0.3) = 0.3016$ and $D(0.4) = 0.4396$ yr^{-2}.
In figure 2 we give a plot of $\ddot{\theta}^{\,\mathrm{TIDE}}(\theta_0 + \dot{\theta}_0 t, t)$ for $e = 0.2056$, $\theta_0 = 2.0$, $\dot{\theta}_0 = 29.0$, the latter two values being (almost arbitrarily) chosen to approximate a solution starting from an angular velocity slightly greater than n. Note that $\ddot{\theta}^{\,\mathrm{TIDE}} \in [-0.19, 0.19]$, which is consistent with the estimate, from equation (4), of $[-0.21, 0.21]$ when $e = 0.2056$.

3.3 The tidal acceleration

We now discuss the tidal acceleration $\ddot{\theta}^{\,\mathrm{TIDE}}(\dot{\theta})$. Throughout this section, we take $e = 0.2056$. Figures 3–5 show the tidal acceleration, plotted vertically, versus the relative rate of rotation, $\dot{\theta}/n$.
This function is illustrated in Figure 3, which shows $\ddot{\theta}^{\,\mathrm{TIDE}}(\dot{\theta})$, plotted over the entire range of interest, $\dot{\theta}/n \in [-1, 5]$. The dominant features here are the 'kinks', which occur at $\dot{\theta}/n = 1 + q/2$ for $q = -1, \ldots, 7$, this being the range of the sum defining the tidal acceleration.
The five 'kinks' at which $\ddot{\theta}^{\,\mathrm{TIDE}}$ changes sign are those corresponding to $q = -1, \ldots 3$, and, for the purpose of comparison, these are plotted over the same narrow range of $\dot{\theta}/n = 1 + q/2 \pm 10^{-4}$, and on the same vertical scale, $\pm 7 \times 10^{-4}$, in figure 4.
The fact that $\ddot{\theta}^{\,\mathrm{TIDE}}$ is continuous, even at a kink, is implied in figure 5, in which $\ddot{\theta}^{\,\mathrm{TIDE}}$ has been plotted against $\dot{\theta}/n$ for $\dot{\theta}/n \in [3/2 - 4 \times 10^{-5},\ 3/2 + 4 \times 10^{-5}]$. However, the derivative $n\,\mathrm{d}\ddot{\theta}^{\,\mathrm{TIDE}}/\mathrm{d}\dot{\theta}$ displays a cusp

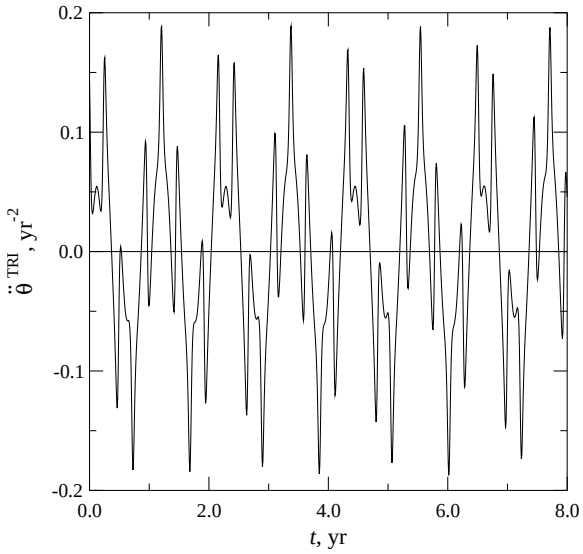

Figure 2: An illustrative plot of the triaxiality angular acceleration, $\ddot{\theta}^{\,\mathrm{TRI}}(\dot{\theta})$ as a function of time, with $e = 0.2056$, and $\theta(t) = 2 + 29t$.

at the values of $\dot{\theta}/n$ corresponding to a kink, as is apparent from the definition of $Q_2(\omega_{lmpq})$ in equation (N.15 mod.), in particular from its dependence on $\chi = |\omega_{220q}| = |2\dot{\theta} - (q+2)n|$. This is illustrated in figure 6.

4 A fast algorithm

We find several different solutions to the differential equation (3), which one is observed depending on the initial conditions. As well as periodic solutions, some of the solutions we find appear, numerically at least, not to be simply periodic — we shall have more to say about these solutions in [Bartuccelli et al. (in preparation)]. Here, we just point out that we distinguish the different captured solutions from each other solely by their mean $\dot{\theta}$ values, $\langle\dot{\theta}\rangle$, defined by $\langle\dot{\theta}\rangle = \lim_{T\to\infty} T^{-1}\int_0^T \dot{\theta}(t)dt$; and that capture can take place in solutions for which a term in the sum (N.10), the triaxiality torque, is approximately zero, *i.e.* for $\theta \approx (q+2)nt/2$, $q \in \mathcal{Q}^{\mathrm{TRI}}$. Hence, we only expect solutions for which $\langle\dot{\theta}/n\rangle \approx -1, -1/2, 1/2, \ldots, 7/2$ and 4.

In order to compute probabilities of capture by the different solutions, with small confidence intervals, via Monte Carlo simulation, many solutions to equation (3), starting from random initial conditions in the set $\mathcal{Q} = [0,\pi] \times [\dot{\theta}_{\min}, \dot{\theta}_{\max}]$, must be computed. Many are needed because, for a given confidence level, the width of the confidence interval is proportional to $I^{-1/2}$, where I is the number of solutions computed: more simulations narrow the confidence interval, but rather slowly.

We take $\mathcal{Q} = [0,\pi] \times [0, 5n]$ in what follows. The triaxiality acceleration depends on 2θ and so we need only consider $\theta_0 \in [0,\pi]$; and the right-most kink is at $\dot{\theta} = 9n/2$, so we choose the maximum value of $\dot{\theta}_0$ to be somewhat greater than this.

We now describe a fast algorithm for solving equation (3), which is based on the high-order Euler method (HEM), described in detail in [Bartuccelli et al. (2015)]. This method has to be adapted for the NFME model because of the discontinuities in the second derivative of $\ddot{\theta}^{\,\mathrm{TIDE}}(\dot{\theta})$ — that is, at the centres of the kinks — that occur at $\dot{\theta}/n = 1/2, 1, 3/2, \ldots, 9/2$. The adaptation we use requires that the subset $\mathcal{Q}$ of the $(\theta, \dot{\theta})$ phase plane be split into strips, all with $\theta \in [0,\pi)$, but with a variety of ranges of $\dot{\theta}$. This splitting is needed in order to meet the error criterion — see below. A strip can be of type H (HEM), when it is far enough removed from the kinks that the HEM can be used; and type N (Numerical), surrounding a kink, where a suitable numerical method has to be used. In a type N strip, there is a possibility that the ODE is stiff, and the numerical method

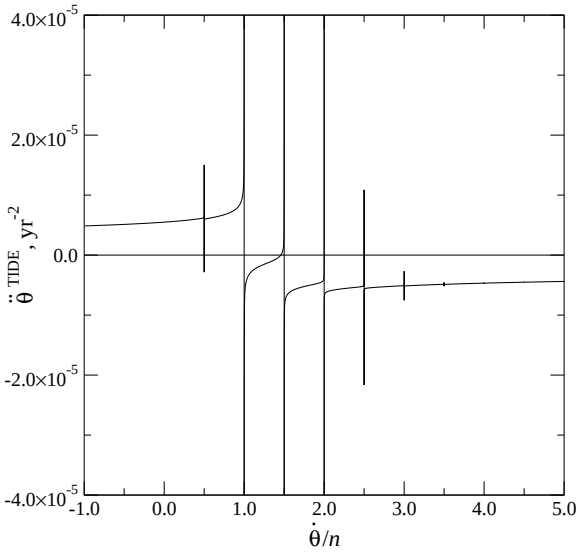

Figure 3: The tidal angular acceleration, $\ddot{\theta}^{\,\mathrm{TIDE}}(\dot{\theta})$, with $e = 0.2056$, as given by equation (2). 'Kinks' occur at values $\dot{\theta}/n = 1/2, 1, 3/2, 2, \ldots, 9/2$, although those at $4, 9/2$ are too small to see on this scale. Note that the angular acceleration does not change sign at a kink for $\dot{\theta}/n = 3, 7/2, 4, 9/2$.

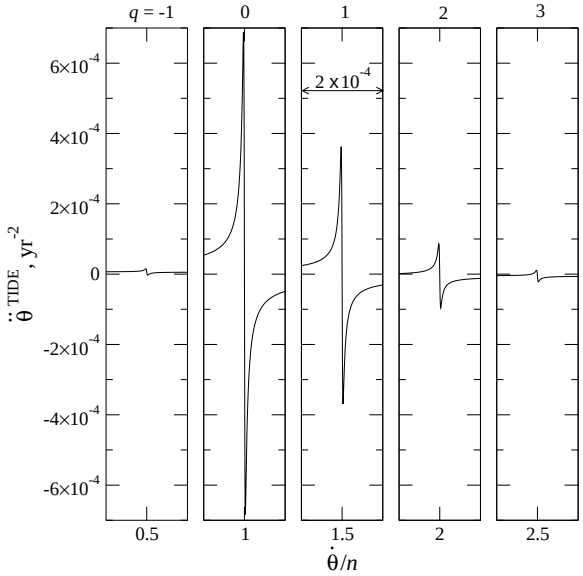

Figure 4: Magnified version of the 'kinks' corresponding to $q = -1, 0, 1, 2, 3$, as shown in figure 3. The width of each plot is 2×10^{-4} and the vertical range is $\pm 7 \times 10^{-4}$ yr^{-2}.

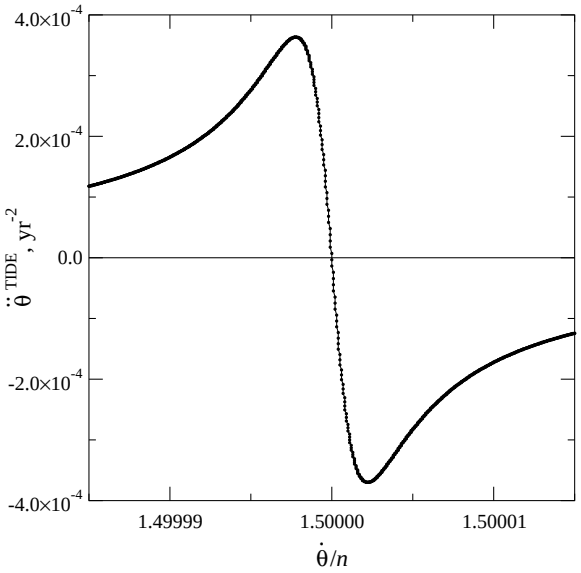

Figure 5: Further magnified version of the 'kink' around $\dot{\theta}/n = 3/2$, suggesting that the derivative is finite for all values of $\dot{\theta}/n$.

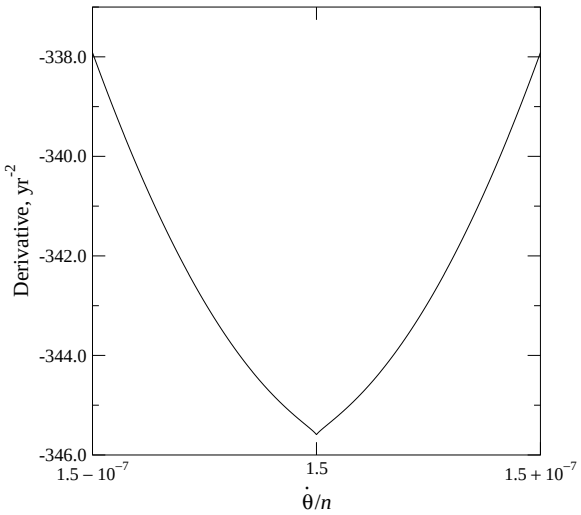

Figure 6: The derivative of the tidal angular acceleration with respect to the relative rate of rotation, that is, $n\,\mathrm{d}\ddot{\theta}^{\,\mathrm{TIDE}}/\mathrm{d}\dot{\theta}$, showing the cusp at $\dot{\theta}/n = 3/2$.

chosen should take this into account.

The detail of this splitting is given in figure 7, in which $\dot{\theta}/n$ is plotted horizontally, with type H regions being shown as continuous lines, type N as dashed lines. The strips are grouped into ten bands, one band covering the region between two kinks. For instance, Band 0 consists of four type H strips, centred on $\dot{\theta}/n = 0.1, 0.275, 0.39$ and 0.45 and with widths $0.2, 0.15, 0.08$ and 0.04 respectively; and one type N strip, where $\dot{\theta}/n \in [0.47, 0.5]$, $\dot{\theta} = 0.5n$ being the position of the first kink. The reasoning behind the choice of these values is given in sections 4.1 and 4.2. The expansion point θ_e for the series solution is always the centre of the strip, and is shown by 'x' in figure 7.

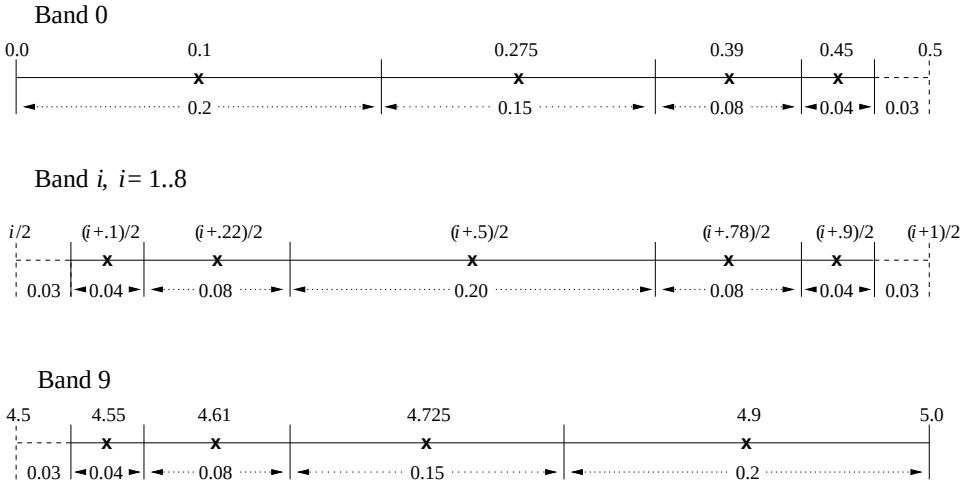

Figure 7: The different strips used for H (HEM, solid line) and N (numerical, dashed line) computation. Numerical values of $\dot{\theta}/n$ are shown. A 'x' shows the expansion point for a series solution. The width of a region in terms of $\dot{\theta}/n$ over which the series solution is valid, for all θ, to within the error bounds (see text) is shown below the line. The strips are grouped into bands. In Bands 0 and 9 there are four H strips and one N strip; in the remaining bands, there are five H, and two N strips.

4.1 Region H: HEM applies

The HEM, which is a fixed timestep implementation of the Frobenius method, can in principle be used to solve equation (3) in regions of the phase plane, $(\theta, \dot{\theta})$, where the functions $\ddot{\theta}^{\,\mathrm{TRI}}$ and $\ddot{\theta}^{\,\mathrm{TIDE}}$ are analytic. From its definition, $\ddot{\theta}^{\,\mathrm{TRI}}(\theta, t)$ is an entire function, so this is no bar to using the HEM. However, $\ddot{\theta}^{\,\mathrm{TIDE}}(\dot{\theta})$ is C^1 in $\dot{\theta}$, with its second derivative being undefined at $\dot{\theta}/n = 1/2, 1, 3/2, \ldots, 9/2$. Hence we approximate $\ddot{\theta}^{\,\mathrm{TIDE}}$ by its Taylor series of degree D_{TID} about a point $\dot{\theta} = \dot{\theta}_e$, bearing in mind that this will only be good for values of $\dot{\theta}$ far from the kinks. In the work reported here, our error criterion (see below) is satisfied with $D_{\mathrm{TID}} = 25$ for all strips.

With these provisos, the HEM works well. We briefly review the method here; full details can be found in [Bartuccelli et al. (2015)].

Let the state vector $\mathbf{x}(t) = \Big(\theta(t), \dot{\theta}(t)\Big)$ and define $t_i = ih,\ i \in \mathbb{N}_0$ where $h > 0$ is a timestep. The ODE allows us to compute, recursively, derivatives of $\theta(t)$ of all orders, far from the kinks. Let the j-th time derivative of $\theta(t)$ be written as $\theta^{(j)}(t)$. We then write the degree-D_s series solution to equation (3) as

$$\mathbf{x}(t_i) = \mathbf{p}_i\left(\mathbf{x}(t_{i-1})\right) = \mathbf{x}(t_{i-1}) + \sum_{j=1}^{D_s} \frac{h^j}{j!}\mathbf{f}_j\left(\mathbf{x}(t_{i-1}), t_{i-1}\right) + O\left(h^{D_s+1}\right) \tag{5}$$

where $D_s > 1$ ($D_s = 1$ gives the Euler method), and $\mathbf{f}_j(\mathbf{x}, t) = \big(\theta^{(j)}(t),\, \theta^{(j+1)}(t)\big)$. Note that $\mathbf{f}(\mathbf{x}, t)$ depends on t as well as $\mathbf{x}$ because the ODE is non-autonomous. For the same reason, $\mathbf{p}$ depends on i. To satisfy the error criterion, the following values of D_s are used in the various bands:

Band	0	1	2	3	4	5	6	7	8	9
D_s	16	15	15	14	14	14	15	16	17	17

Equation (5) allows us to advance the solution by a time h. Our immediate objective, however, is to compute the Poincaré map for the ODE in an efficient way. Let us denote the period in t of $\ddot{\theta}^{\,\mathrm{TRI}}$ as $T_0 = 2\pi/n$ (which is one 'Mercury year'), and put $\mathbf{x}_k = \mathbf{x}(kT_0)$. Then the Poincaré map, $\mathbf{P}$, is defined by $\mathbf{x}_{k+1} = \mathbf{P}(\mathbf{x}_k)$. Iteration

of $\mathbf{P}$ many times starting from a given initial condition $\mathbf{x}_0 = (\theta(0), \dot{\theta}(0))$ enables us to generate a sequence of 'snapshots' of the state variables as the system evolves, from which we can deduce the attractor in which the system is eventually captured. For details of capture detection, see below. Using a large number I of initial conditions, one can then estimate the probability of capture in any of the possible steady-state solutions.
In order to satisfy the error criterion, timestep h needs to be sufficiently small. As with all the parameters mentioned so far, there is a trade-off between speed and accuracy; a choice of $h = T_0/M$ with $M = 24$ is a good compromise in practice. Finally, then, the map $\mathbf{P}$ can be built up from the functions $\mathbf{p}_i$ by $\mathbf{P}(\mathbf{x}) = \mathbf{p}_M \circ \mathbf{p}_{M-1} \circ \ldots \circ \mathbf{p}_1(\mathbf{x})$, and this is the HEM.
The expressions for $\mathbf{p}_i$ are derived by computer algebra and are initially very large, but most of the terms are negligible and hence can be pruned away. By 'term' we mean here a polynomial in $\dot{\theta}$ — these are then multiplied by powers of $\sin 2\theta, \cos 2\theta$ in order to make up $\mathbf{p}_i$. In practice, every term whose magnitude is less than 10^{-16} at the largest and smallest values of $\dot{\theta}$ within a strip is deleted. The value of 10^{-16} is chosen because the usual double precision arithmetic is carried out to around 16 significant figures. The resulting expression is then converted to Horner form [Press et al. (1992)] for efficient evaluation. Typically, after pruning has been carried out, the expressions for $\mathbf{p}_i$ contain 20 – 35 terms and are of the form: θ-component $= \theta + r_3 + sr_5 + cr'_5 + scr_4 + s^2 r_2$, $\dot{\theta}$-component $= r'_4 + sr_6 + cr'_6 + scr''_4 + s^2 r'''_4 + s^2 cr_1 + s^3 r'_1$, where r_k, r'_k etc. are polynomials in $\dot{\theta}(t_{i-1})$ of degree k, and $s = \sin 2\theta$, $c = \cos 2\theta$.
We now describe the error criterion used. The final version of the code for computing the Poincaré map via the HEM is compared to a high-accuracy, standard numerical computation of the same thing. The full expression for $\ddot{\theta}^{\,\mathrm{TIDE}}$ is used in the accurate numerical computation, not its series approximation. The numerical algorithm used is the standard Runge-Kutta method as implemented in the computer algebra software Maple, computing to 25 significant figures and with absolute and relative error tolerances of 10^{-15}. The numerical and HEM computations of $\mathbf{P}(\mathbf{x})$ are then compared, for each of the type H strips, using 250 uniformly distributed random values of $\mathbf{x}$ in each strip. The comparison gives the maximum value of the modulus of the difference between each component, computed both ways, over the 250 random points. The maximum difference observed over all strips is assumed to be representative of the overall maximum difference. Its values are about 3×10^{-14}, 1.4×10^{-13} in the θ- and $\dot{\theta}$-components respectively.

4.2 Region N: numerical method must be used

From figure 7, it can be seen that the HEM can be used for about 89% of $\dot{\theta} \in [0, 5n]$, but in the strips surrounding the kinks, $\theta \in [0, \pi)$, $\dot{\theta}/n \in [(q+2)/2 - 0.03, (q+2)/2 + 0.03]$, $q \in \mathcal{Q}^{\mathrm{TIDE}}$, the type N strips, a purely numerical method has to be used.
It is possible that the ODE may be stiff here, so we choose two numerical methods and compare the results. The methods used are: (1) an explicit Runge-Kutta (RK) method due to Dormand and Price, as described in [Hairer et al. (1993)], and (2) the Adams method/Backward Differentiation Formulae (BDF) [Radhakrishnan and Hindmarsh (1993)], with the ability to switch automatically between them. The Adams method is an explicit predictor-corrector method, which, along with RK, is suitable for non-stiff problems, whereas BDF is suitable for stiff problems.
In practice, with the parameters in Table 1, BDF is rarely needed, so the comparison between (1) and (2) above comes down to comparing the RK and Adams methods. The implementation of Adams used [Radhakrishnan and Hindmarsh (1993)] is approximately 1.6 times slower than RK for this problem, but the probabilities obtained from integration starting from the same 3200 random points in $\mathcal{Q}$ are in good agreement — see Table 2 — so, for type N strips, we choose RK, for which we fix both the absolute and relative error tolerances to be 2×10^{-14}. This value is chosen to be comparable with the error entailed by polynomial interpolation — see below.
The probabilities obtained are not identical, neither should we expect them to be. The long-term fate of a given trajectory depends very sensitively on the details of its computation, implemented for very long integration times. What is important in the end is the probabilities obtained, and Table 2 shows these to be robust against the algorithm used to solve the ODE.
Computation time can be saved by efficient calculation of $\ddot{\theta}^{\,\mathrm{TRI}}$ and $\ddot{\theta}^{\,\mathrm{TIDE}}$. The expression for $\ddot{\theta}^{\,\mathrm{TRI}}$ can be

Runge-Kutta			Adams		
$\langle\dot{\theta}/n\rangle$	Probability, %	95% c.i.	$\langle\dot{\theta}/n\rangle$	Probability, %	95% c.i.
1/2	0.8125	0.3110	1/2	0.8750	0.3227
1	27.44	1.546	1	27.38	1.545
3/2	43.44	1.717	3/2	43.81	1.719
2	22.03	1.436	2	21.91	1.433
5/2	5.063	0.7596	5/2	5.094	0.7618
3	1.094	0.3604	3	0.750	0.2989
7/2	0.031	(0.0612)	7/2	0.094	(0.1060)
4	0.094	(0.1060)	4	0.094	(0.1060)

Table 2: Comparison of probability of capture by the eight attractors with $\langle\dot{\theta}/n\rangle = 1/2, 1, \ldots, 4$. These were computed using the Runge-Kutta and the Adams method in N-type strips, with HEM being used elsewhere. The same 3200 uniformly distributed random initial conditions were used in both cases. Confidence intervals in brackets are unreliable since there are too few data points in the case of these attractors.

converted into a polynomial of degree 1 in $\cos 2\theta$ and $\sin 2\theta$, and degree 8 in $\cos nt/2$ and $\sin nt/2$. In Horner form, this polynomial can be evaluated efficiently, using 2 sin/cos evaluations, 16 addition and 36 multiplication operations.

Evaluation of $\ddot{\theta}^{\,\mathrm{TIDE}}(\dot{\theta})$ in the obvious way is computationally expensive, since it requires the calculation of one fractional power per term in equation (N.11b) — nine in all. A more efficient way to evaluate it is:

Case 1: if $\dot{\theta}$ is far from a kink, then use a pre-computed Chebyshev polynomial fit [Press et al. (1992)] to $\ddot{\theta}^{\,\mathrm{TIDE}}$ — the function is very smooth here;

Case 2: if $\dot{\theta}$ is close to a kink, compute the contribution to $\ddot{\theta}^{\,\mathrm{TIDE}}$ from that kink exactly, according to the appropriate single term in the sum (N.11b), with the effect of the remaining kinks being replaced by a Chebyshev polynomial fit.

Hence, at most one fractional power is computed per evaluation of $\ddot{\theta}^{\,\mathrm{TIDE}}$. In practice, we use a polynomial only (Case 1 above), of degree 25, unless $2\dot{\theta}/n$ is within ± 0.08 of an integer, when Case 2 applies. In Case 2, we use a polynomial of degree 7 to fit the remaining terms. The resulting absolute error is no more than 4×10^{-14}. For comparison, the ratio of the CPU time taken to evaluate $\ddot{\theta}^{\,\mathrm{TIDE}}$ directly, and via polynomial fitting, is about 5.1.

A comparison of the timings in different circumstances is given in Table 3, for which 1000 random initial conditions were used. The CPU time taken to iterate $\mathbf{P}$ 10^5 times starting from each of these was measured, with any data in which the trajectory moved from a type H strip to one of type N, or vice versa, being rejected.

Method	Strip	Mean time for 10^5 iterations of $\mathbf{P}$, CPU-sec
Runge-Kutta, slow $\ddot{\theta}^{\,\mathrm{TIDE}}$	N	61.1
Runge-Kutta, fast $\ddot{\theta}^{\,\mathrm{TIDE}}$	N	20.5
HEM	H	0.313

Table 3: Timings for the computation of 10^5 iterations of the Poincaré map, $\mathbf{P}$, in various circumstances. These are: type H or type N strips, and, in type N strips, with or without the fast computation of $\ddot{\theta}^{\,\mathrm{TIDE}}$ described in section 4.2. The mean was taken over 895/105 random initial conditions for type H/N strips respectively.

4.3 Capture test

We now describe the test used to detect capture of a solution. Figure 8 shows $\dot{\theta}_k = \dot{\theta}(kT_0)$ plotted against k for $0 \leq k \leq 7.8 \times 10^6$. In this case, the initial condition was $\mathbf{x}_0 = (0, 49)$ and capture took place after about 7.7×10^6 iterations of the Poincaré map, which corresponds to $7.7 \times 10^6 T_0 = 1.85 \times 10^6$ yr.
There are several ways that capture could be detected. We choose to divide the $\dot{\theta}_k$ dataset into blocks of length L and compute the least squares gradient of each block. As can be seen from figure 8, this gradient will be negative pre-capture, and close to zero post-capture.

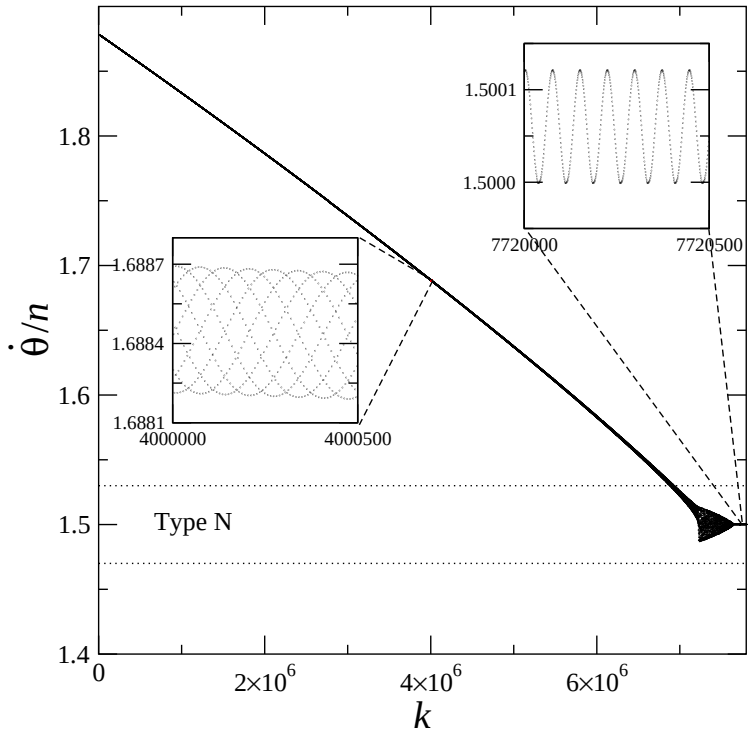

Figure 8: An illustration of capture dynamics: $\dot{\theta}_k$, with initial condition $\mathbf{x}_0 = (0, 49) = (0, 1.878n)$, is plotted against k, for $0 \leq k \leq 7.8 \times 10^6$. In this case, capture takes place in a solution with $\langle \dot{\theta}/n \rangle \approx 3/2$. Two small regions are shown on a magnified scale. On the left, we see the pre-capture dynamics and on the right, post-capture. The HEM was used for all computations outside the strip $1.47 \leq \dot{\theta}/n \leq 1.53$, marked 'Type N'.

In detail the test is as follows. Let $\bar{y}_j$ be the mean value of $\dot{\theta}_k/n$ over the j-th block of length L, and let m_j be the least squares gradient of $\dot{\theta}_k$ plotted against k in block j. Capture is deemed to have taken place when

$$|2\bar{y}_j - [2\bar{y}_j]| < \varepsilon_i \quad \text{and} \quad |m_j| < \varepsilon_m \quad \text{for } K \text{ successive blocks.}$$

Here, $[x]$ is the nearest integer to x, and the factor of two occurs in the first expression because capture can take place at integer or half-integer values of $\dot{\theta}/n$. In practice, we choose $L = 10,000$, $K = 8$, $\varepsilon_i = 10^{-3}$ and $\varepsilon_m = 3 \times 10^{-7}$. The speed of a probability computation depends on the choice of these parameters.
Figure 9 shows a typical plot of m_j versus block number j, from $j = 0$ until capture, which takes place at $j = 770$.

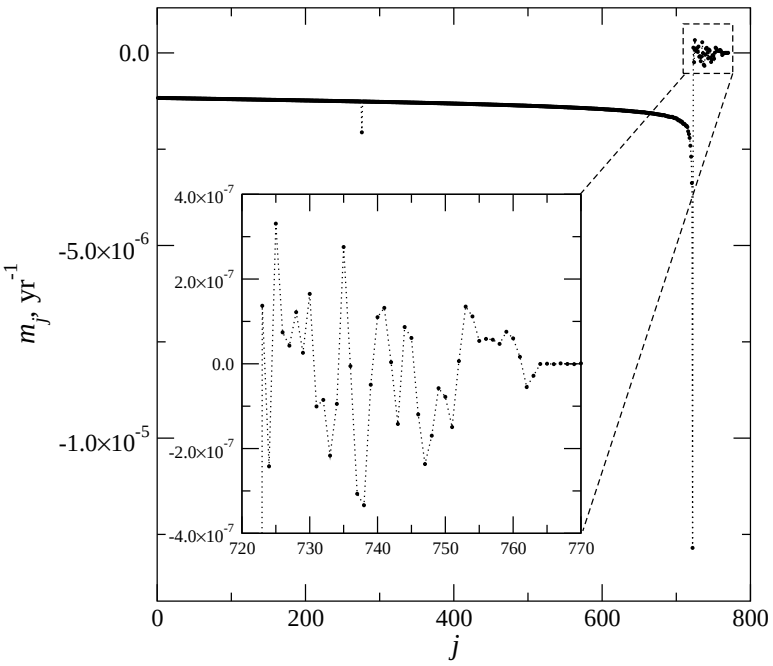

Figure 9: An illustration of the capture test in practice. The least-squares gradient of $\dot{\theta}_k$, m_j, versus the block number, j, for the trajectory in figure 8. Blocks are of length 10,000 iterations of the Poincaré map and if one of the criteria for capture is that $|m_j| < 3 \times 10^{-8}$ for eight successive blocks, then this happens in blocks 763–770 inclusive. Hence, capture in this case is detected after 7.7×10^6 iterations of the Poincaré map.

5 An illustrative probability of capture computation

To illustrate how the foregoing works in practice, and to show some timings, we now give results of a calculation of probability of capture for the parameters in Table 1.

As in [Bartuccelli et al. (2015)], we use the CPU-sec as a unit of time, which is defined in terms of the following sum:

$$S(m) = \sum_{i=1}^{m} \frac{(i+1)(i+3)}{i(i+2)(i+4)(i+6)},$$

whose evaluation requires $5m$ multiplications and $6m-1$ additions. We define 1 CPU-sec to be the CPU time taken to evaluate $S(N_c)$, where $N_c = 5.96 \times 10^7$, which is the CPU time taken to do this computation on the computer used to do some of the calculations in this paper. The time taken can vary according to circumstances, e.g. the loading, the type of processor and so on. Hence, care has to be taken in the codes to scale the CPU-sec appropriately for the particular hardware used: the computation of $S(N_c)$ is timed after every successful capture, and the CPU-sec scaling factor is updated on each occasion.

One other point to note is that a computation of probability is trivial to parallelise. The initial conditions in $\mathcal{Q}$ are generated by a pseudo-random number generator, and a different sequence of pseudo-random numbers can be produced just by changing the seed. Hence, by running N copies of the program on N separate processors with N different seeds, N times the number of initial conditions can be investigated at the same time.

The CPU time taken to integrate until capture depends strongly on the initial condition, and in particular, the proportion of the integration that is carried out in type N strips (which is a slow process) as opposed to type H strips (where it is fast). By considering 57,600 random initial conditions, we find the following:

Mean time to capture: 1156 CPU-sec, with standard deviation 1190 CPU-sec

Maximum time to capture: 5161 CPU-sec; minimum time to capture: 1.188 CPU-sec.

Total iterations in type N strips: $\sim 1.6 \times 10^{11}$; total iterations in type H strips: $\sim 1.2 \times 10^{12}$.

From the above, we see that overall, about 1.4×10^{12} iterations of the Poincaré map were needed to estimate the probability of capture for 57,600 initial conditions, and that 12% of these were in type N strips, with the remaining 88% being in type H strips. These values have a sensitive dependence on the capture parameters.
We can now estimate the factor by which our approach speeds up a typical probability of capture computation. Let $T_{\text{mix}}(n)$ be the CPU time taken to iterate the Poincaré map n times using HEM in type H strips and the chosen numerical method in type N strips, and let $T_{\text{num}}(n)$ be the time taken when using the numerical method everywhere. Then, using the data above and from Table 3, we estimate that

$$\frac{T_{\text{mix}}(n)}{T_{\text{num}}(n)} \approx \frac{n(0.12 \times 20.5 + 0.88 \times 0.313)10^{-5}}{20.5n \times 10^{-5}} \approx \frac{2}{15}.$$

Our approach therefore speeds up this computation by a factor of about 7.5.
A histogram of capture times is given in figure 10. Let $\tau(\mathbf{x}_0)$ be the number of CPU-sec required to iterate the Poincaré map, starting from $\mathbf{x}_0$, until the capture criterion of section 4.3 is met. In order to produce Figure 10, 57,600 random values of $\mathbf{x}_0 \in \mathcal{Q}$ were generated and $\tau(\mathbf{x}_0)$ was computed for each. This figure is a histogram of the proportions of the values of $\tau(\mathbf{x}_0)$ that lie in the ranges 0–200, 200–400, ..., 4800–5000 CPU-sec.
Finally, we give an estimate of the probabilities themselves in Table 4. The 95%-confidence interval [Walpole et al. (1998)] is defined such that the probability of capture in a given attractor A lies in the interval $[\hat{p} - \Delta p, \hat{p} + \Delta p]$, with 95% confidence. Here, $\Delta p = 1.96\sqrt{\hat{p}(1-\hat{p})/I}$, in which $I = 5.76 \times 10^4$ is the number of initial conditions and $\hat{p}$ is the proportion of these initial conditions that end up in A. For these values, in the worst case, which is $\hat{p} = 1/2$, $\Delta p \approx 0.41\%$.

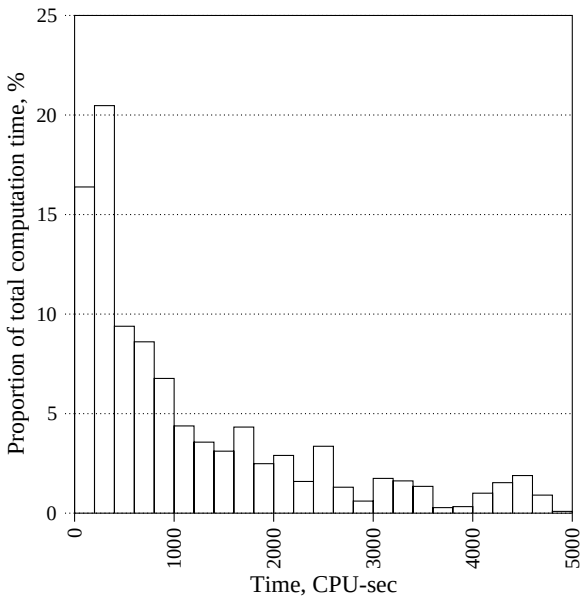

Figure 10: Histogram showing the probability that the computation time for iteration to capture lies in various ranges. The interpretation is that, for instance, a CPU time of between 0 and 200 CPU-sec is required to establish the capture of about 16.3% of trajectories (leftmost bar). Four values of CPU-time > 5000 CPU-sec were excluded from the histogram and so the dataset contains 57 596 points. The modal value of CPU-time is in the range 200–400 CPU-sec.

p/q	Number	Probability, $\hat{p}$, %	95% c.i.
1/2	349	0.6059	0.063
2	16292	28.285	0.368
3/2	24344	42.264	0.403
4	13252	23.007	0.344
5/2	2775	4.8177	0.175
6	473	0.8212	0.074
7/2	89	0.1545	0.032
8	26	0.0451	0.017
9/2	0	0.0000	0.000

Table 4: Probability of capture by various attractors with $\langle \dot{\theta}/n \rangle = 1/2, 1, \ldots, 4$; as expected, 9/2 was never observed. These were computed using the Runge-Kutta method [Hairer et al. (1993)] in N-type strips, with HEM being used elsewhere. We used 57,600 uniformly distributed random initial conditions in $\mathcal{Q} = [0, \pi] \times [0, 5n]$.

6 Conclusions

It was not the main purpose of this paper to give results of the computation of probabilities of capture for various sets of parameters — rather, we wanted to show how this computation, in the case of constant eccentricity e, can be accelerated. This requires us to solve the ODE (3), and bearing in mind that this is periodic in time with period $T_0 = 2\pi/n$, our objective is to compute the Poincaré map, which advances the state variables $\mathbf{x} = (\theta, \dot{\theta})$ by a time T_0, as fast as possible. This enables us to generate a sequence of values $\mathbf{x}_k$, from which salient information about the dynamics can be deduced.

The dissipation term, $\ddot{\theta}^{\,\mathrm{TIDE}}(\dot{\theta})$, which is a C^1 function of the angular velocity $\dot{\theta}$, and additionally varies rapidly in the ranges of $\dot{\theta}$ around the so-called 'kinks', complicates the computation, and requires the use of a standard numerical ODE solver for some of the time. We point out ways in which these purely numerical computations can be carried out efficiently, by streamlining the calculation of the triaxiality and tidal accelerations. However, in about 88% of the phase plane the high-order Euler method [Bartuccelli et al. (2015)] can be used, and this speeds up the computation significantly.

The present case should be contrasted with the constant time lag model, in which dissipation is just proportional to $\dot{\theta} - \omega$ with ω a constant. In the light of its simplicity, this has been used in many publications, for instance, [Bartuccelli et al. (2015)] and references therein. In that case, only a single set of integrators $\mathbf{p}_i$, defined in equation (5), was needed to build up the Poincaré map. In other words, there was only one strip, which was the whole of $\mathcal{Q}$, and the HEM could be used everywhere.

Compare that with the current case using the parameters in Table 1. Here, $\mathcal{Q}$ has to be divided into 48 strips and an integrator set up for each. Setting up the codes for the HEM in each strip, which is done by computer algebra, itself takes significant time, but the pay-off is an increase in speed by a factor of approximately 65 in the strips where HEM can be used, compared to using a standard numerical method.

A probability of capture computation requires a capture detection algorithm, and one has been described. It is based on the fact that after capture, the angular velocity has no underlying decay: a captured solution has a close to constant mean value of $\dot{\theta}_k = \dot{\theta}(kT_0)$ for all k greater than the value at which capture takes place. Typically, the mean is taken over 10^4 successive k values.

A test run of our algorithm, in which 57,600 initial conditions were iterated until capture took place, reveals that the overall speed of computation is faster by a factor of about 7.5 compared to using a standard numerical algorithm alone.

An important question left unanswered in this paper is 'What is the nature of the solutions in which capture takes place?' The answer turns out to be more complicated than expected: periodic solutions with mean $\dot{\theta}/n \approx -1, -1/2, 1/2, \ldots, 4$ have been computed (high-accuracy numerics are needed). There is also numerical evidence for the existence of attracting solutions whose period is not a small integer multiple of T_0.

The dynamics of solutions to equation (3), both pre- and post-capture, will be subject of a future publication [Bartuccelli et al. (in preparation)].

References

[Bartuccelli et al. (in preparation)] M.V. Bartuccelli, J.H.B. Deane and G. Gentile, *Dynamics of the spin orbit equation of Makarov et al. with constant eccentricity,* In preparation, 2016.

[Bartuccelli et al. (2015)] M.V. Bartuccelli, J.H.B. Deane and G. Gentile, *The high-order Euler method and the spin-orbit model: a fast algorithm for solving differential equations with small, smooth nonlinearity*, Celestial Mechanics and Dynamical Astronomy, vol 121, Issue 3, March 2015, pp 233 – 260. `http://doi 10.1007/s10569-014-9599-7`

[Celletti and Chierchia (2008)] A. Celletti, L. Chierchia, *Measures of basins of attraction in spin-orbit dynamics*, Celestial Mechanics and Dynamical Astronomy, **101**, no. 1-2, 159–170 (2008)

[Celletti and Chierchia (2009)] A. Celletti, L. Chierchia, *Quasi-periodic attractors in celestial mechanics* Arch. Ration. Mech. Anal. **191**, no. 2, 311–345 (2009)

[Correia and Laskar (2004)] A.C.M. Correia, J. Laskar, *Mercury's capture into the 3/2 spin-orbit resonance as a result of its chaotic dynamics* Nature **429**, 848–850 (2004)

[Duriez (2007)] L. Duriez *Cours de mécanique Céleste classique*, `http://lal.univ-lille1.fr/mecacel_duriez/CoursMCecr_Duriez.pdf`

[Goldreich and Peale (1966)] P. Goldreich, S. Peale, *Spin-orbit coupling in the solar system*, Astronom. J. **71**, no. 6, 425–438 (1966)

[Hairer et al. (1993)] E. Hairer, S.P. Nørsett and G. Wanner, *Solving Ordinary Differential Equations I. Non-stiff problems*, ISBN 978-3-540-56670-0, Second Revised Edition, Springer Series in Computational Mathematics, Springer-Verlag, Berlin and Heidelberg (1993)
Code available from `http://www.unige.ch/~hairer/software.html`

[Jorba and Zou (2005)] À. Jorba and M. Zou, *A software package for the numerical integration of ODEs by means of high-order Taylor methods*, Experimental Mathematics 14, pp. 99–117 (2005)

[Makarov et al. (2012)] V.V. Makarov, C. Berghea and M. Efroimsky, *Dynamical evolution and spin-orbit resonances of potentially habitable exoplanets: the case of GJ 581d*, Astrophys. J., **761**, no. 2, 83 (2012)

[Makarov (2012)] V.V. Makarov, *Conditions of passage and entrapment of terrestrial planets in spin-orbit resonances*, Astrophys. J., **752**, no. 1, 73 (2012)

[Noyelles et al. (2014)] B. Noyelles, J. Frouard, V.V. Makarov and M. Efroimsky, *Spin-orbit evolution of Mercury revisited*, Icarus **241**, 26-44 (2014)

[Press et al. (1992)] W.H. Press, S.A. Teukolsky, W.T. Vetterling and B.P. Flannery, *Numerical Recipes in C*, ISBN 0-521-43108-5, Cambridge University Press, Cambridge, UK (1992)

[Radhakrishnan and Hindmarsh (1993)] K. Radhakrishnan and A.C. Hindmarsh, *Description and Use of LSODE, the Livermore Solver for Ordinary Differential Equations*, NASA Reference Publication 1327, Lawrence Livermore National Laboratory Report **UCRL-ID-113855** `https://computation.llnl.gov/casc/nsde/pubs/u113855.pdf`
Code available from `http://lh3lh3.users.sourceforge.net/solveode.shtml`

[Walpole et al. (1998)] R.E. Walpole, R.H. Myers and S.L. Myers, *Probability and Statistics for Engineers and Scientists* ISBN 0-13-840208-9, Prentice Hall, Upper Saddle River, NJ (1998)